

An ocean large-eddy simulation model with application to deep convection in the Greenland Sea

Donald W. Denbo and Eric D. Skyllingstad

Pacific Northwest National Laboratory, Sequim, Washington

Abstract. A nonhydrostatic, Boussinesq, three-dimensional model, the ocean large-eddy simulation model (OLEM), has been developed to study deep oceanic convection. The model uses a subgrid-scale parameterization of turbulence developed for large-eddy simulation models, and the advection of scalars is accomplished using a monotonic scheme. A set of experiments was performed using OLEM to provide a direct comparison with laboratory results and aircraft measurements of the atmospheric convective boundary layer. The results from these experiments are in excellent agreement with laboratory and atmospheric convective boundary layer measurements of the mean profiles of zonal and vertical velocity variance, potential temperature variance, and heat flux. The horizontal wavenumber spectra of zonal and vertical velocity are also in good agreement with laboratory measurements and Kolmogorov's theoretical inertial subrange spectrum. A set of experiments using a potential temperature-salinity profile from the central Greenland Sea for model initialization was conducted to study the effect of the thermobaric instability and rotation on the structure and evolution of deep oceanic convection. The artificial removal of the thermobaric instability suppresses penetrative convection, which is responsible for rapid changes in water properties at depths much greater than occurs for convective, mixed-layer deepening. The vertical velocity and diameter, -0.08 m s^{-1} and 300 m, respectively, of the penetrative plumes are in good agreement with observations from the Greenland Sea. A period of strong penetrative convection is followed by a gradual transition to convective, mixed-layer deepening. During penetrative convection the values of heat flux are about 2 times greater than convective, mixed-layer deepening. In the absence of rotation the evolution of penetrative convection occurs more rapidly, and vertical motions are more vigorous. The presence of the horizontal component of rotation forces asymmetries in the circulation around a penetrative plume. These experiments clearly demonstrate the importance of thermobaric instability and rotation on deep convection. To properly model large-scale flows in regions of penetrative convection, it is necessary to include these effects in the vertical mixing parameterization.

1. Introduction

High-latitude deep water production is an important link in the global thermohaline circulation. Observations and model studies suggest that variations in deep water production can have a significant impact on the global climate by altering the transportation and storage of heat and CO_2 in the deep ocean. For example, in a coupled general circulation model calculation by *Washington and Meehl* [1989], elevated levels of atmospheric CO_2 caused increases in precipitation, sea surface temperatures, and the hydrostatic stability of the surface layer at high latitudes of each hemisphere. Consequently, the meridional thermohaline circulation was weakened. Were such a change to occur during a global warming episode, the reduced meridional circulation would limit the poleward heat transport and tend to stabilize the degree of warming in polar regions (i.e., produce a negative feedback). A similar "thermohaline catastrophe" with two stable modes is suggested by the modeling results of *Manabe and Stouffer* [1988]. Because of the strong influence deep water production can have on the ocean circulation, a good understanding of the processes responsible for deep water formation is important for modeling the global ocean-atmosphere system.

Deep water is produced by two main processes, one driven by brine rejection from ice-covered shelf regions and the other by open-water deep convection that is forced by heat loss, evaporation, and brine rejection. The topic of this paper centers on the simulation of open-water convection, without the influence of shelf topography or ice-related processes. The majority of open-water convection occurs during wintertime storms when high winds coupled with low atmospheric temperatures lead to strong surface sensible and latent heat loss. Estimates of deep water production from open-water convection range from 0.5 to 1.2 Sv ($1 \text{ Sv} = 10^6 \text{ m}^3 \text{ s}^{-1}$) for the Greenland Sea [*Heinze et al.*, 1990; *Rhein*, 1991], 3.9 Sv for the Labrador Sea [*Clarke and Gascard*, 1983], and 1.6 to 3.2 Sv for the Weddell Sea [*Gordon*, 1982].

On the basis of observations from the Golfe du Lion region of the Mediterranean Sea, *Killworth* [1976] describes a simple conceptual model of convection with the following three phases: preconditioning, violent mixing, and dispersal through sinking and spreading. Preconditioning describes the doming of isopycnal surfaces by cyclonic circulation and moderate surface cooling. The violent mixing phase begins with the formation of numerous small-scale convective plumes that can reach to the ocean bottom. During the violent mixing phase a region of well-mixed water develops with a horizontal scale of 10–100 km. This region is commonly referred to as a "chimney." About a month after the violent mixing phase, horizontal mixing by baroclinic eddies completes the process with the breakup of the chimney structure.

Copyright 1996 by the American Geophysical Union.

Paper number 95JC02828.
0148-0227/96/95CJ-02828\$05.00

Here we are interested in simulating the violent mixing phase of the convection process. It is during this stage that the ocean behaves much like a convective atmospheric boundary layer with strong vertical motions, large heat and momentum transports, and chaotic motion fields.

Only limited measurements of polar convective plumes exist because of the random behavior of convection and the harsh surface conditions that are associated with convective events. *Gascard and Clarke* [1983] reported on a mesoscale homogenous area in the Labrador Sea where plumes are generally less than 1 km in scale, with vertical motions ranging up to 9 cm s^{-1} . *Schott et al.* [1993] have reported plume events in the central Greenland Sea that propagate downward at 8 cm s^{-1} with a diameter of 350 m. Other observations by *Rudels et al.* [1989] in the Greenland Sea and *Gordon* [1978] in the Weddell Sea present the vertical structure of temperature and salinity after a convective event has occurred, without information on the convection process. Until more extensive measurements are performed, numerical models can provide a useful tool for understanding the physical processes active in convective events.

Laboratory work on convection and convective turbulence in the presence of rotation have been reported by *Fernando et al.* [1989, 1991], *Boufnov and Golitsyn* [1990], and *Maxworthy and Narimousa* [1994]. These studies have been very helpful in understanding how rotation and buoyancy forcing combine to set the velocity and length scales. These experiments do not, however, explore the effect of thermobaricity on convection.

Until recently, numerical models of oceanic convection have been limited to a one-dimensional framework with uniform mixing when an unstable profile exists. For example, *Killworth* [1976, 1979] applied a multilayered, one-dimensional model to simulate a convective chimney in the Weddell Sea. We apply a three-dimensional, large-eddy simulation (LES) model that simulates the mixing process by generating eddies with scales comparable to the mixed-layer depth. LES models have been successful in simulating the atmospheric boundary layer [e.g., *Deardorff*, 1980; *Moeng*, 1984; *Schmidt and Schumann*, 1989; *Mason*, 1994]. However, their application in the ocean has been limited [*McWilliams et al.*, 1993; *Garwood et al.*, 1994; *Siegel and Domaradzki*, 1994; *Skyllingstad and Denbo*, 1995]. The model we developed is based on the *Deardorff* [1980] set of nonhydrostatic equations with a subgrid-scale parameterization of turbulence that depends on a turbulent kinetic energy budget. Our modeling approach is similar to the work presented by *Jones and Marshall* [1993], although their efforts were more focused on chimney-scale convection using an idealized vertical temperature profile, constant eddy diffusivity, and an isolated region of surface cooling. *Raasch and Etling* [1991] have applied an LES model to study rotating thermal convection, but without specific application to the ocean.

An important aspect of our oceanic version of a LES model is the inclusion of a realistic nonlinear equation of state for seawater. This addition is important because of the thermobaric effect, which can enhance convection in high-latitude waters. Variations in the compressibility of seawater with pressure and temperature are the cause of the thermobaric effect. For example, when relatively cold, fresh water is displaced downward into relatively warm, salty water, it becomes denser than the surrounding deep water because of the thermobaric effect. The thermobaric density change is a function of overall water temperature, with cold water showing a stronger density variation with depth than warm water. For these reasons, the thermobaric effect is particularly important in cold, polar waters, where runoff and ice melt during spring and summer produces a surface layer that is fresher than the underlying deep

water [*Aagaard and Carmack*, 1989]. Furthermore, *Killworth* [1976] demonstrated that inclusion of the thermobaric effect can determine whether convection will even occur, and *Garwood et al.* [1994] has shown that the inclusion of thermobaricity causes a middepth maximum in the turbulent kinetic energy and buoyancy flux. The relationship between density and salinity is also important when two water types of differing salinity are mixed, leading to an increase in the density of the resulting water. This process is known as cabbeling. With convection the entrainment of ambient seawater into a descending plume can lead to a density increase from cabbeling [*McDougall*, 1987].

In this paper we examine the convection process for the central Greenland Sea. The Greenland Sea experiments provide a physically based analysis of the convection process and give insight on how small-scale convective features can generate deep mixing in the ocean. As shown by our results, the thermobaric properties of seawater can generate convective plumes that penetrate into stably stratified water. This is an important result that could indicate a major defect in convective parameterizations that are currently used in large-scale ocean circulation models.

The paper begins with a description of the three-dimensional model used in the experiments. Next, the model is verified by comparing a simple mixed-layer simulation with laboratory data from *Deardorff and Willis* [1985]. Following the verification test, an ocean simulation case is presented. We conclude the paper with a summary of the results and a short discussion on improving convective parameterizations in ocean general circulation models.

2. Model Description

Defining the scales of motion in a geophysical fluid problem is a fundamental step in selecting the appropriate formulation for a numerical model. The length scales and timescales of oceanic deep convection require a model that encompasses motions that are smaller and of higher frequency than is acceptable for existing ocean models. For example, previous model studies of convective effects have routinely applied the hydrostatic approximation in the model formulation [*Killworth*, 1979; *Madec et al.*, 1991]. When a model uses the hydrostatic assumption, convection is not directly simulated but is parameterized by assuming a mixed-layer entrainment or a simple layer-averaging process whenever adjacent levels are unstable. When rotation is important, $(H/l_p)^2 \ll 1$ is required in order to apply the hydrostatic approximation [*Jones and Marshall*, 1993], where H is the vertical length scale and l_p is the horizontal length scale (the deformation radius). In the experiments conducted here this ratio varies from 4 to 11.

It is also important to accurately separate the resolved-scale processes from motions that cannot be simulated at the chosen resolution. Typically, the unresolved motions, also known as the inertial subrange, are parameterized by an eddy viscosity that is dependent on a turbulent energy budget. In the *Deardorff* [1980] model used here a prognostic equation for subgrid-scale turbulent kinetic energy is employed. Empirical relationships between the predicted turbulent energy and the eddy coefficients connect the subgrid-scale model to the basic set of equations for the resolved motions.

2.1. Momentum Equations

The ocean large-eddy model (OLEM) described here is nonhydrostatic, Boussinesq, and three-dimensional. The primitive equation model uses a turbulent kinetic energy subgrid model and

monotonic advection scheme. The momentum equations are based on the system presented by *Deardorff* [1980] and *Moeng* [1984]:

$$\frac{\partial u}{\partial t} = -\frac{1}{\rho_0} \frac{\partial P}{\partial x} + R_u, \quad (1)$$

$$\frac{\partial v}{\partial t} = -\frac{1}{\rho_0} \frac{\partial P}{\partial y} + R_v, \quad (2)$$

$$\frac{\partial w}{\partial t} = -\frac{1}{\rho_0} \frac{\partial P}{\partial z} + R_w - \langle R_w \rangle, \quad (3)$$

$$\frac{\partial u}{\partial x} + \frac{\partial v}{\partial y} + \frac{\partial w}{\partial z} = 0, \quad (4)$$

where the velocities u , v , and w are in the x , y , and z (zonal, meridional, and upward) directions, respectively, and where

$$R_u = -u \frac{\partial u}{\partial x} - v \frac{\partial u}{\partial y} - w \frac{\partial u}{\partial z} + 2\Omega_z v - 2\Omega_y w - \frac{\partial}{\partial x}(\overline{u''^2}) - \frac{\partial}{\partial y}(\overline{u''v''}) - \frac{\partial}{\partial z}(\overline{u''w''}),$$

$$R_v = -u \frac{\partial v}{\partial x} - v \frac{\partial v}{\partial y} - w \frac{\partial v}{\partial z} - 2\Omega_z u - \frac{\partial}{\partial x}(\overline{v''u''}) - \frac{\partial}{\partial y}(\overline{v''^2}) - \frac{\partial}{\partial z}(\overline{v''w''}),$$

$$R_w = -u \frac{\partial w}{\partial x} - v \frac{\partial w}{\partial y} - w \frac{\partial w}{\partial z} - g \frac{\rho'}{\rho_0} + 2\Omega_y u - \frac{\partial}{\partial x}(\overline{w''u''}) - \frac{\partial}{\partial y}(\overline{w''v''}) - \frac{\partial}{\partial z}(\overline{w''^2}).$$

The double-primed variables denote subgrid quantities. The angle brackets denote horizontal means, Ω_z and Ω_y are the vertical and horizontal components of the Coriolis parameter, respectively. The Boussinesq approximation is used with density defined as

$$\rho = \bar{\rho} + \rho' \quad (5)$$

where

$$\bar{\rho} = \frac{1}{L_x L_y} \int \int \rho|_{t=0} dx dy, \quad \rho_0 = \frac{1}{L_z} \int \bar{\rho} dz, \quad (6)$$

$\rho = \rho(\Theta, S, P)$, ρ' is the resolved perturbation density, and Θ , S , and P are potential temperature, salinity, and pressure, respectively; L_x , L_y , and L_z are the size of the model domain in the zonal, meridional, and vertical directions, respectively, and

$$\frac{\rho'}{\rho_0} \ll 1. \quad (7)$$

The diagnostic equation for pressure is formed by taking the divergence of the momentum equations (1) thru (3) and then substituting (4) to yield

$$\frac{1}{\rho_0} \nabla^2 P = \frac{\partial}{\partial x} R_u + \frac{\partial}{\partial y} R_v + \frac{\partial}{\partial z} (R_w - \langle R_w \rangle). \quad (8)$$

The evolution of scalars is governed by

$$\frac{\partial \phi}{\partial t} = -u \frac{\partial \phi}{\partial x} - v \frac{\partial \phi}{\partial y} - w \frac{\partial \phi}{\partial z} - \frac{\partial}{\partial x}(\overline{u''\phi''}) - \frac{\partial}{\partial y}(\overline{v''\phi''}) - \frac{\partial}{\partial z}(\overline{w''\phi''}), \quad (9)$$

where ϕ can be Θ , S , or a tracer.

2.2. Subgrid Model

The subgrid-scale turbulence parameterization follows the method described by *Deardorff* [1980], where an eddy viscosity scheme is used for fluxes and the eddy coefficient is set proportional to the square root of the subgrid turbulent kinetic energy (TKE). The subgrid TKE is calculated using a prognostic equation (in standard tensor form):

$$\frac{\partial \overline{e''}}{\partial t} = -u_i \frac{\partial \overline{e''}}{\partial x_i} - \overline{u_i'' u_j''} \frac{\partial u_i}{\partial x_j} - \frac{g}{\rho_0} \overline{w'' \rho''} - \frac{\partial}{\partial x_i} \left[\overline{u_i'' \left(e'' + \frac{p''}{\rho_0} \right)} \right] - \varepsilon \quad (10)$$

where $e'' = 1/2(u''^2 + v''^2 + w''^2)$ is the subgrid TKE and ε is the dissipation rate of e'' .

The subgrid fluxes are defined as

$$\overline{u_i'' u_j''} = -K_m \left(\frac{\partial u_i}{\partial x_j} + \frac{\partial u_j}{\partial x_i} \right) + \frac{2}{3} \delta_{ij} \overline{e''}, \quad (11a)$$

$$\overline{u_i'' \phi''} = -K_h \frac{\partial \phi}{\partial x_i}, \quad (11b)$$

$$\overline{u_i'' \left(e'' + \frac{p''}{\rho_0} \right)} = -C_{dg} K_m \frac{\partial \overline{e''}}{\partial x_i}, \quad (12)$$

where ϕ denotes scalar quantities such as S or Θ . The eddy coefficients are defined as

$$K_m = C_{km} \lambda e''^{1/2}, \quad K_h = (C_{hl} + C_{hs} \frac{\lambda}{\Delta s}) K_m \quad (13)$$

where $\Delta s = (\Delta x \Delta y \Delta z)^{1/3}$ and

$$\lambda = \Delta s, \quad (14a)$$

$$\lambda = C_l e''^{1/2} \left(\frac{g}{\rho_0} \frac{\partial \rho}{\partial z} \right), \quad (14b)$$

for unstable and stable conditions, respectively. The dissipation rate ε is prescribed by

$$\varepsilon = \frac{C}{\lambda} e''^{3/2}$$

and $C = C_{el} + C_{es}(\lambda/\Delta s)$. The empirical constants [*Deardorff*, 1973, 1980] are defined as

$$C_{dg} = 2, \quad C_{el} = 0.19, \quad C_{es} = 0.51, \quad C_l = 0.76, \\ C_{km} = 0.1, \quad C_{hl} = 1, \quad C_{hs} = 2. \quad (15)$$

In the grid points next to the solid boundaries, C is increased by a factor of 3.9 to compensate for boundary effects [*Deardorff*, 1980].

Mason [1994], in a critical review of LES techniques, found that those models that used different subgrid parameterizations and numerical methods produced differences in the vertical velocity variance that were comparable to the subgrid variance. During the testing of OLEM the resolved motions were insensitive to variations of the subgrid turbulent parameterization empirical constants.

2.3. Expanded Model Equations

Defining a modified pressure as $\tilde{P} = P/\rho_0 + (2/3)e''$ and substituting (11) into (1) thru (3) yields

$$\frac{\partial u}{\partial t} = -\frac{\partial \tilde{P}}{\partial x} + R_u, \quad (16)$$

$$\frac{\partial v}{\partial t} = -\frac{\partial \tilde{P}}{\partial y} + R_v, \quad (17)$$

$$\frac{\partial w}{\partial t} = -\frac{\partial \tilde{P}}{\partial z} + R_w - \langle R_w \rangle, \quad (18)$$

where

$$\begin{aligned}
 R_u &= -u \frac{\partial u}{\partial x} - v \frac{\partial u}{\partial y} - w \frac{\partial u}{\partial z} + 2\Omega_z v - 2\Omega_y w \\
 &\quad + 2 \frac{\partial}{\partial x} \left(K_m \frac{\partial u}{\partial x} \right) + \frac{\partial}{\partial y} \left[K_m \left(\frac{\partial u}{\partial y} + \frac{\partial v}{\partial x} \right) \right] + \frac{\partial}{\partial z} \left[K_m \left(\frac{\partial u}{\partial z} + \frac{\partial w}{\partial x} \right) \right], \\
 R_v &= -u \frac{\partial v}{\partial x} - v \frac{\partial v}{\partial y} - w \frac{\partial v}{\partial z} - 2\Omega_z u \\
 &\quad + \frac{\partial}{\partial x} \left[K_m \left(\frac{\partial u}{\partial y} + \frac{\partial v}{\partial x} \right) \right] + 2 \frac{\partial}{\partial y} \left(K_m \frac{\partial v}{\partial y} \right) + \frac{\partial}{\partial z} \left[K_m \left(\frac{\partial v}{\partial z} + \frac{\partial w}{\partial y} \right) \right], \\
 R_w &= -u \frac{\partial w}{\partial x} - v \frac{\partial w}{\partial y} - w \frac{\partial w}{\partial z} - \frac{g}{\rho_*} \rho' + 2\Omega_y u \\
 &\quad + \frac{\partial}{\partial x} \left[K_m \left(\frac{\partial u}{\partial z} + \frac{\partial w}{\partial x} \right) \right] + \frac{\partial}{\partial y} \left[K_m \left(\frac{\partial v}{\partial z} + \frac{\partial w}{\partial y} \right) \right] + 2 \frac{\partial}{\partial z} \left(K_m \frac{\partial w}{\partial z} \right).
 \end{aligned}$$

Substituting (11) into (9) yields

$$\begin{aligned}
 \frac{\partial \Phi}{\partial t} &= -u \frac{\partial \Phi}{\partial x} - v \frac{\partial \Phi}{\partial y} - w \frac{\partial \Phi}{\partial z} \\
 &\quad + \frac{\partial}{\partial x} \left(K_h \frac{\partial \Phi}{\partial x} \right) + \frac{\partial}{\partial y} \left(K_h \frac{\partial \Phi}{\partial y} \right) + \frac{\partial}{\partial z} \left(K_h \frac{\partial \Phi}{\partial z} \right). \quad (19)
 \end{aligned}$$

2.4. Numerics and Boundary Conditions

OLEM uses a three-dimensional, staggered grid with pressure and scalars in the center of a cube and the velocity components on the faces (Figure 1). The coordinate system origin is in the lower, left front corner of the domain. Grid spacing in the model is uniform with $\Delta x = \Delta y = \Delta z$. This is not a severe limitation, given the scale of problems for which OLEM is best suited.

The boundary conditions used with OLEM were chosen to be consistent with the assumption that the model domain, horizontal scale of a few kilometers, is being placed in a region that is horizontally homogeneous at scales many times larger than the model domain. The horizontal boundary conditions were therefore chosen to be cyclic, where flow out a horizontal boundary enters the opposite boundary. We make the rigid lid approximation and use a flat bottom,

$$w = 0, \quad z = 0, L_z. \quad (20)$$

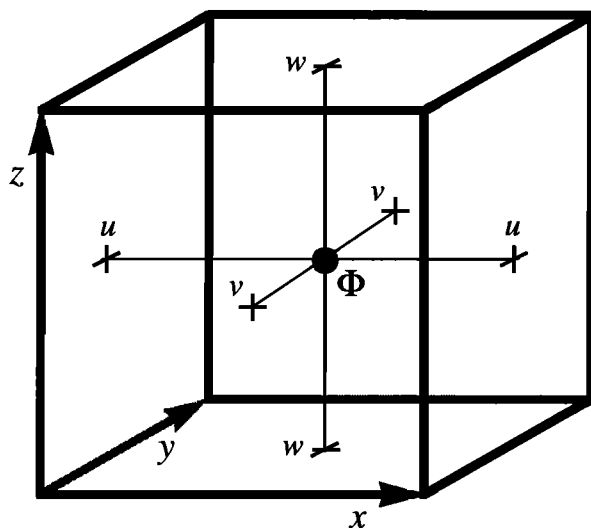


Figure 1. The model grid structure which is cubic and the u , v , and w velocity components centered on the east-west, north-south, and top-bottom faces. Potential temperature, salinity, and subgrid turbulent kinetic energy, scalars denoted by Φ , are located in the center of the cube.

The surface boundary conditions, $z = L_z$, for the surface fluxes use a formulation where the fluxes directly force the surface grid cell. The surface boundary conditions for horizontal velocity components, Θ , and S , are

$$u^{n+1} = u^n + \frac{2\Delta t \tau_x}{\Delta z \bar{\rho}}, \quad (21)$$

$$v^{n+1} = v^n + \frac{2\Delta t \tau_y}{\Delta z \bar{\rho}}, \quad (22)$$

$$\Theta^{n+1} = \Theta^n + \frac{\Delta t H_f}{\Delta z c_p \bar{\rho}}, \quad (23)$$

$$S^{n+1} = S^n - \frac{\rho}{\rho + \frac{\Delta t L_f}{\Delta z L_v}} \quad (24)$$

where τ_x , τ_y , H_f , and L_f are the zonal wind stress, meridional wind stress, total heat flux, and latent heat flux, respectively. The superscripts on the model variables denote the current time step number, where Δt is the time step increment. The vertical derivatives of u , v , w , Θ , and S in (16) thru (19) are set to zero at $z = L_z$. The values of specific heat c_p and latent heat of vaporization L_v are chosen for seawater at 10°C, 35 practical salinity units (psu), and atmospheric pressure. The bottom boundary conditions, $z = 0$, are no-slip for the horizontal velocities and no-flux for Θ and S .

To ensure incompressibility, the Poisson equation for pressure is solved by applying the numerical divergence to the numerical form of the equation after Moeng [1984], Deardorff [1973], and Harlow and Welch [1965],

$$\begin{aligned}
 \nabla^2 \tilde{p} &= \frac{\partial}{\partial x} R_u + \frac{\partial}{\partial y} R_v + \frac{\partial}{\partial z} (R_w - \langle R_w \rangle) \\
 &\quad + \frac{1}{6} \left(\frac{\partial u}{\partial x} + \frac{\partial v}{\partial y} + \frac{\partial w}{\partial z} \right) / \Delta t. \quad (25)
 \end{aligned}$$

This correction is included to remove any accumulation of errors during the calculation of pressure due to round-off or truncation. The control of the nonphysical $2\Delta x$ motions is accomplished by applying a Shapiro filter to all three velocity components. In this study a sixth-order Shapiro filter, with the highest-order term of ∇^{12} , was applied in all three directions every third time step.

The accurate advection of Θ and S is very important in OLEM. Small errors in advecting these two components of density can result in significant errors in the resultant density field and velocity perturbations that are of the same magnitude as the motions of interest. Therefore the advection of Θ , S , e'' , and tracers is accomplished using a monotonic scheme based on the work of Colella [1990] using the flux limiting step from van Leer [1977]. This scheme has the property that strong fronts of the advected quality, after a small amount of numerical diffusion, reach an equilibrium shape that is then transported without significant additional numerical diffusion.

3. Model Validation

Three experiments were performed to provide direct comparisons with laboratory experiments of Willis and Deardorff [1974] and Deardorff and Willis [1985], as well as with aircraft measurements of the atmospheric boundary layer by Lenschow et al. [1980]. The initial conditions for these experiments were a constant potential temperature of 5.5°C in the upper 450 m with a linear potential temperature gradient of $3.2 \times 10^{-4} \text{°C m}^{-1}$ below (Figure 2). Salinity was held constant at 35 psu in these experiments to avoid the effects of thermobaricity and cabbeling

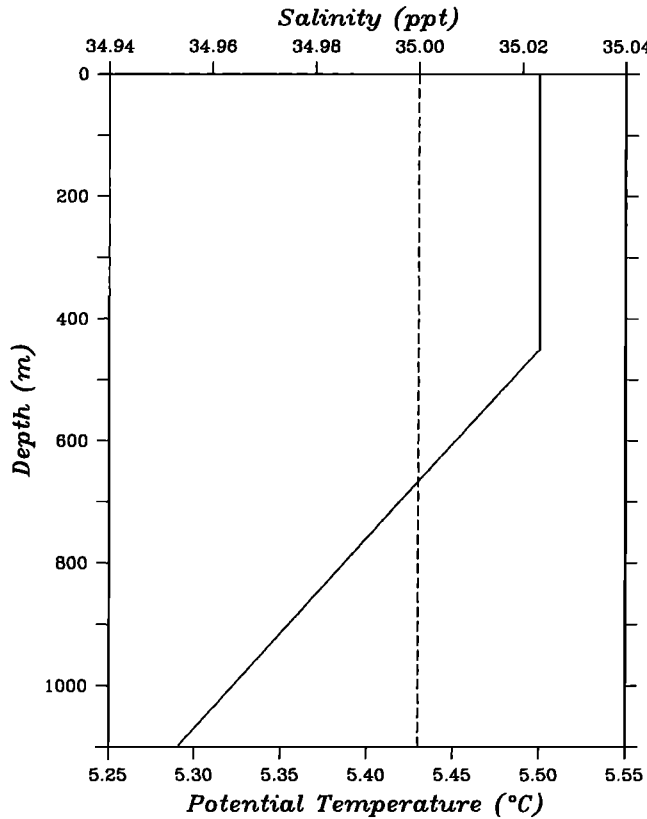


Figure 2. Initial potential temperature (solid line) and salinity (dashed line) profile used with the model validation experiments.

and to allow a direct comparison with the measurements. The grid spacing was 30 m, with a $128 \times 128 \times 34$ grid, yielding a domain size of 3840 m in the zonal and meridional directions and 1020 m in the vertical. The time step was 90 s, with a run length of 5 days, for a total of 4800 time steps. The surface forcing included a heat flux of -300 W m^{-2} , no wind stress, and no latent heat flux (no evaporation). Model spin-up was facilitated by adding a spatially random pattern of heat flux, with a maximum amplitude of 90 W m^{-2} , to the heat flux during the first 2 hours. The inclusion of planetary rotation via the Coriolis force is the only difference among the three experiments (Table 1). The experiment names are expressed by run series-experiment designation, where run series can be validation (V) or Greenland Sea (GS), and experiment designation is full rotation (FR), no rotation (NR), vertical component of rotation (VCR), or no thermobaric instability (NTB). The first experiment includes both the vertical and horizontal components of rotation (V-FR), the second does not include rotation (V-NR), and the third includes only the vertical component of rotation (V-VCR). A latitude of 75°N was chosen for the two experiments with rotation.

Table 1. Validation Experiment Summary

Experiment	$\Omega_z \equiv 0$	$\Omega_y \equiv 0$	Comments
V-FR	no	no	full rotation (FR)
V-NR	yes	yes	no rotation (NR)
V-VCR	yes	no	vertical component of rotation (VCR)

Here Ω_z and Ω_y denote the vertical and horizontal components of the Coriolis parameter, respectively.

Table 2. Scales and Nondimensional Numbers for the V-FR and V-VCR Experiments for Day 3

Variable	Value
z_i , m	615
z_c , m	2231
D , m	1709
l_p , m	329
$(z_i/l_p)^2$	3.5
T_* , $^\circ\text{C}$	0.002
Ra_f	9×10^7
Ta	4×10^6
w_* , m s^{-1}	0.037
u_v , m s^{-1}	0.098
Ro^*	0.29
K_m , $\text{m}^2 \text{s}^{-1}$	0.025
K_h , $\text{m}^2 \text{s}^{-1}$	0.075
α , $^\circ\text{C}^{-1}$	1.19×10^{-4}
β , psu^{-1}	7.7×10^{-4}
ρ_0 , kg m^{-3}	1027.62

Conditions on day 3 were as follows: buoyancy flux $B_0 = 8.47 \times 10^{-8} \text{ m}^2 \text{s}^{-3}$, Coriolis parameter $f = 1.4 \times 10^{-4} \text{ s}^{-1}$, reference potential temperature $\Theta_0 = 5.5^\circ\text{C}$, and reference salinity $S_0 = 35 \text{ psu}$.

We find that according to the nomenclature of *Boubnov and Golitsyn* [1990], the values of the flux Rayleigh number, $Ra_f = B_0 z_i^4 / (K_h^2 K_m)$, and Taylor number, $Ta = f^2 z_i^4 / K_m^2$, place the validation experiments with rotation, V-FR and V-VCR, in the geostrophic turbulence regime (Table 2), where $B_0 = (g/\rho_0)(\alpha H_f/c_p + \beta S_0 L_f/L_v)$ is the buoyancy flux and z_i is the mixed-layer depth. The thermal expansion α and salinity contraction β coefficients are determined, for the purposes estimating the buoyancy flux only, from a linearized equation of state of seawater

$$\rho = \rho_0 [1 - \alpha(\Theta - \Theta_0) + \beta(S - S_0)],$$

where $\rho_0 = \rho(\Theta_0, S_0, P_0)$, Θ_0 , S_0 , and $P_0 \equiv 0$ are the reference density, potential temperature, salinity, and pressure, respectively. The values of K_m and K_h are computed by averaging over the mixed-layer depth and the horizontal extent of the model domain. The depth of the heat flux minimum (Figure 3) was chosen as the mixed-layer depth.

Fernando et al. [1991] and *Maxworthy and Narimousa* [1994], in their laboratory experiments of rotating convection, found that rotational effects dominated the turbulence for mixed-layer depths z_i greater than the transition depth $z_c \approx 12.7(B_0/f^3)^{1/2}$. *Maxworthy and Narimousa* [1994] found that when rotational effects dominate, the appropriate velocity and length scale are the maximum swirl velocity of an individual vortex, $u_v \approx 4.0 \sqrt{B_0/f}$, and the diameter of the circle of maximum velocity, $D \approx 5.2(B_0 z_i^2/f^3)^{1/4}$, respectively. The horizontal length scale (deformation radius) for rotating convection defined by *Jones and Marshall* [1993] is $l \equiv D/5.2$. In addition to z_c , the “natural” Rossby number, $Ro^* = [B_0/(f^3 z_i^2)]^{1/2}$, a characteristic of the flow based on the vortex velocity introduced by *Maxworthy and Narimousa* [1994], has been used to measure the importance of rotation [*Jones and Marshall*, 1993]. The natural Rossby number can be rewritten in terms of z_c , $Ro^* = 0.079(z_c/z_i)$.

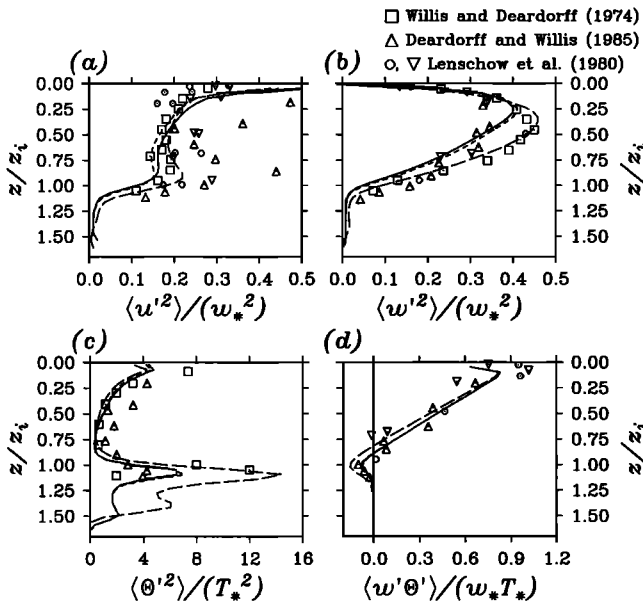


Figure 3. Vertical profiles of horizontally averaged and normalized (a) zonal velocity variance $\langle u'^2 \rangle$, (b) vertical velocity variance $\langle w'^2 \rangle$, (c) temperature variance $\langle \Theta'^2 \rangle$, and (d) heat flux $\langle w'\Theta' \rangle$, for the three validation (V) experiments; V-FR (solid line), V-NR (long-dashed line), and V-VCR (short-dashed line), where FR is full rotation, NR is no rotation, and VCR is vertical component of rotation. The profiles are normalized using the vertical velocity scale w_* , the temperature scale T_* , and the mixed-layer depths $z_i = 615, 645$, and 615 m for the V-FR, V-NR, and V-VCR experiments, respectively. The profiles were produced by averaging over a period of 1 day centered on day 3, and error bars corresponding to ± 1 standard deviation are included for vertical velocity variance in Figure 3b. The laboratory measurements of Willis and Deardorff [1974], case S1, and of Deardorff and Willis [1985] are denoted by squares and triangles, respectively. Aircraft measurements by Lenschow et al. [1980] are denoted by circles for February 24, 1975, and inverted triangles for February 16, 1975.

Since the value of z_c is several times larger than z_i (Table 2), we conclude that convection is not dominated by rotation for the validation experiments, and consequently, u_v and D are not the appropriate scales for velocity and space. For convection in the absence of rotation the model studies of Deardorff [1972] and Wyngaard et al. [1974] show that the scales for velocity, temperature, and distance in the mixed layer are $w_* = (B_0 z_i)^{1/3}$, $T_* = (1/\rho_0 c_p)(H_f/w_*)$, and z_p , the mixed-layer depth, respectively.

When rotation is not important, $(H/l)^2 \ll 1$ is required in order to apply the hydrostatic approximation [Jones and Marshall, 1993], where H and l are the vertical and horizontal length scales, respectively. Since both H and l scale with z_i for convective mixed-layer deepening, we find that $(H/l)^2 \approx 1$; thus the hydrostatic approximation is not valid for the model validation experiments.

3.1. Instantaneous Fields

The three-dimensional structure of Θ for the V-FR experiment at 3 days is illustrated in Plate 1. At the surface, cold water collects at lines of horizontal convergence and is advected downward by the downdrafts. Internal waves, forced by the convection, create undulations of the mixed-layer base. At the peaks of these waves, cold water is often advected upward and entrained into the mixed

layer. The regions of warmer water at the mixed-layer base indicate where strong downdrafts are pushing warm water below the base.

The horizontal structure of Θ , w , and e'' for model day 3 is presented for the V-FR (Plate 2a) and V-NR (Plate 2b) experiments at depths $z/z_i = 0.21, 0.62, 0.965$. The instantaneous fields for the V-VCR experiment are not presented because they are very similar to those of the V-FR experiment, both qualitatively and quantitatively. In general, the width of the convective elements increases and the vertical velocity decreases with depth. There is a general decrease in e'' from the surface where buoyancy forcing is strongest for both experiments. However, there is an increase in e'' for V-NR near the mixed-layer base from the shear created when the downdrafts impact the pycnocline. The increased e'' from the surface is transported by the convection throughout the mixed layer, but its value is not homogenized, and substantial structure in e'' exists throughout the mixed layer.

The most striking differences between the V-FR and V-NR experiments is the level of organization in the convective structures at $0.21z_p$, most easily seen in w . For V-NR (Plate 2b) the structure is approximately hexagonal, with a diameter of about twice the mixed-layer depth. This structure is modified by the turbulent eddies that are present in the flow. There is also an organized structure for the V-FR (Plate 2a) experiment, but here the addition of rotation forces strong, sinuous downdrafts that surround regions of weaker upwelling. For V-FR these structures are up to 2000 m in length but, more typically, are less than 1200 m in length and 150 to 300 m wide. These scales compare favorably to the deformation radius l_p of about 300 m (Table 2). The structures in the V-NR experiment are much larger, with continuous regions of downdrafts of over 3000 m in length and typically 200 to 400 m wide. These structural differences are also evident at $0.62z_p$ and $0.965z_p$, where the downdraft regions are still more organized and stronger for V-NR. Evidence of overshooting convective downdrafts is present for V-NR at $0.965z_p$, as indicated by the centers of strong downward velocity surrounded by relatively strong upward return flow. The return flow is constrained to be near the downdraft by the deflected mixed-layer base.

In general, the Θ structure reflects the w structure; however, at $0.62z_p$, Θ is nearly homogenous in both experiments and only the strongest downdrafts are apparent. The Θ variations at $0.21z_p$ are from the cooled surface water transported by the downdrafts, whereas at $0.965z_p$, the variations are from the colder water below the pycnocline being brought up by the return flow.

3.2. Mean Profiles

Comparison of deep ocean simulation results with laboratory tank data and aircraft measurements is facilitated by using scaled perturbation quantities. Perturbation quantities are defined as $\phi' = \phi - \langle \phi \rangle$. In the convective mixed layer (CML) the mixed-layer depth z_p , the depth where the heat flux is a minimum, emerges as the controlling length scale. Because convection is not strongly affected by rotation, the velocity and temperature scales within the mixed layer are w_* and T_* .

The normalized vertical profiles from model day 3 of $\langle u'^2 \rangle$, zonal velocity variance (Figure 3a), $\langle w'^2 \rangle$, vertical velocity variance (Figure 3b), $\langle \Theta'^2 \rangle$, potential temperature variance (Figure 3c), and $\langle w'\Theta' \rangle$, heat flux, (Figure 3d) show excellent agreement with both laboratory measurements, denoted by the squares and triangles, and aircraft measurements, denoted by the circles and inverted triangles. The V-FR experiment (solid line),

talking about warm plumes overshooting

length: one branch of hexagonal

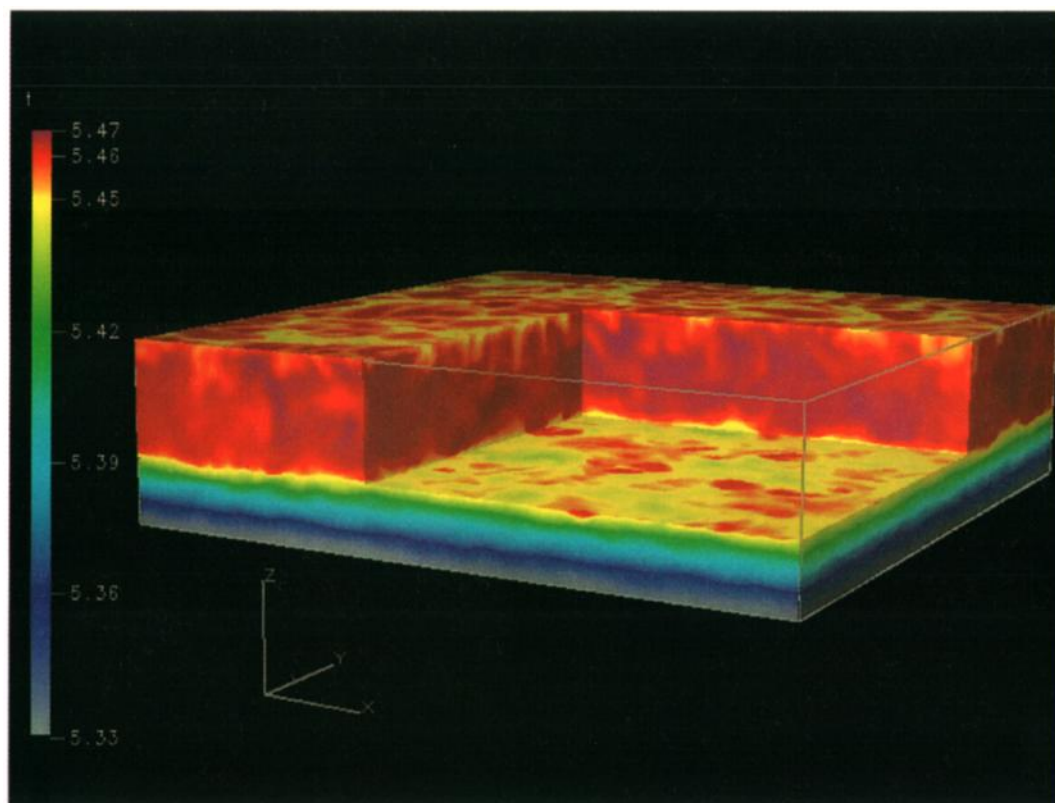


Plate 1. Three-dimensional cutaway view of potential temperature for the validation with full rotation (V-FR) experiment at 3 days. The temperature scale has been adjusted to improve visualization of the mixed layer. The origin is located at the lower, left front corner.

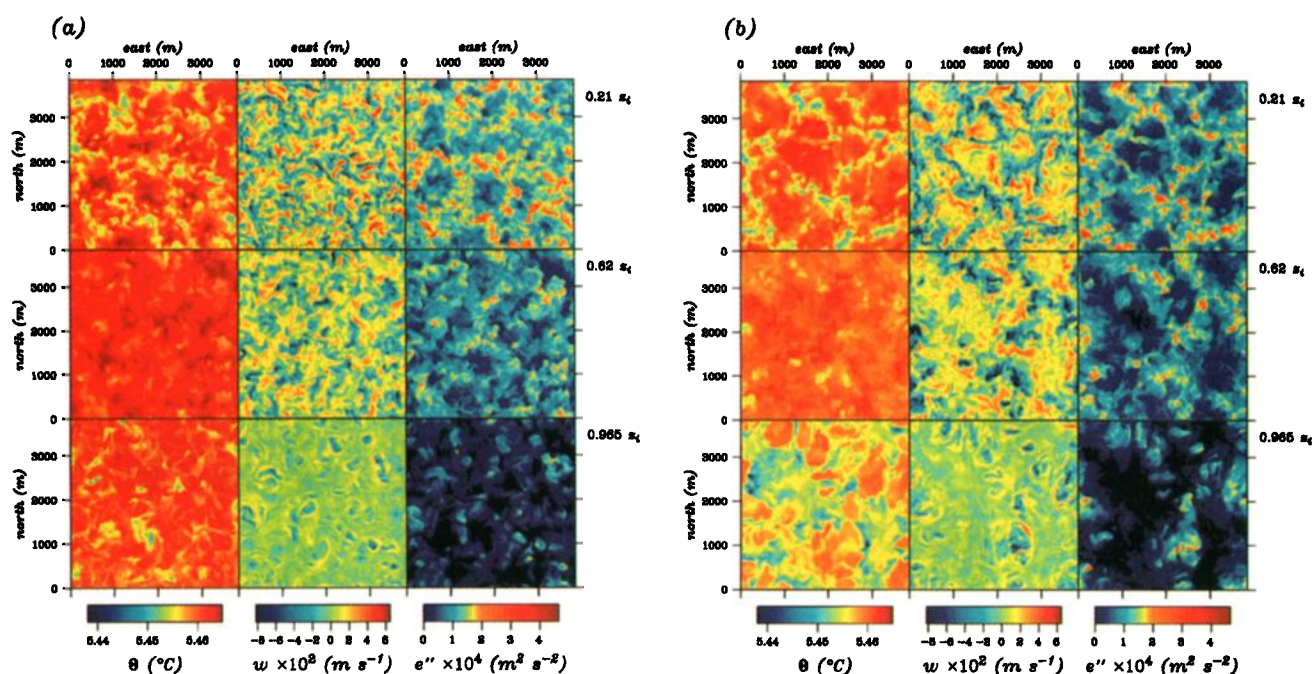


Plate 2. Horizontal sections from the validation experiments, (a) V-FR and (b) V-NR (no rotation) at day 3 of potential temperature Θ , vertical velocity w , and subgrid turbulent kinetic energy e'' , at $z/z_t = 0.965, 0.62$, and 0.21 depths. Here w and e'' have been multiplied by 10^2 and 10^4 , respectively, for display purposes.

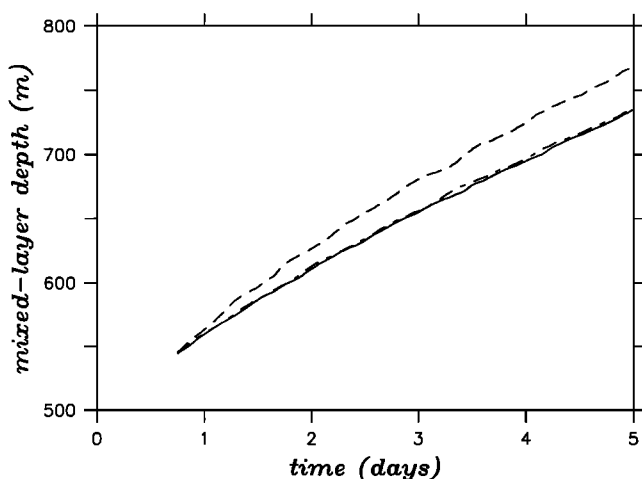


Figure 4. Horizontally averaged mixed-layer depth as a function of time for the three validation experiments; V-FR (solid line), V-NR (long-dashed line), and V-VCR (short-dashed line).

and the V-VCR experiment (short-dashed line) are very similar for all four quantities. The V-NR experiment (long-dashed line), however, has a different character than the V-FR and V-VCR experiments in several instances. The principal differences are (1) the slight peak that occurs for the V-NR experiment in $\langle u'^2 \rangle$ (Figure 3a) just above the base of the mixed layer, (2) significantly larger $\langle w'^2 \rangle$ (Figure 3b) for the V-NR experiment that extends from $0.2z_i$ to the base of the mixed layer, and (3) the larger $\langle \Theta'^2 \rangle$ (Figure 3c) in the V-NR experiment that occurs just below the base

of the mixed layer. These differences are a result of the “damping” effect of rotation, which reduces the strength of vertical motions in the V-FR experiment. The deficit in $\langle \Theta'^2 \rangle$ and $\langle w'\Theta' \rangle$ at the surface (normalized heat flux should be 1) is caused by heat flux being expressed as a potential temperature change in the top grid cell (see (23)). This deficit does not adversely affect the resolved heat and potential temperature fluxes below the top grid cell.

The mixed-layer depth increases more rapidly for the V-NR experiment than for the V-FR and V-VCR experiments (Figure 4), where the change is nearly identical. These differences can also be explained in terms of the more vigorous vertical motions that are present for the V-NR experiment. The stronger vertical motions more quickly erode the mixed-layer base.

3.3. Spectra

The horizontal wavenumber spectra from model day 3 of the zonal velocity component, vertical velocity component, and potential temperature, denoted by Φ_u , Φ_w , and Φ_Θ , respectively, are presented in Figure 5 for the three validation experiments at three levels, $z/z_i = 0.21, 0.62, 0.965$, and for the laboratory measurements of Deardorff and Willis [1985] at levels $z/z_i = 0.21, 0.62, 0.99$. The deepest level for the validation experiments was chosen to ensure that the spectra were computed for a depth that is one grid cell above the base of the mixed layer. The spectra are multiplied by wavenumber, normalized by the convective scales, and then plotted versus kz_i , the normalized wavenumber to facilitate comparison with the laboratory results of Deardorff and Willis [1985]. The above spectra, in the inertial subrange, should follow Kolmogorov’s theoretical spectrum

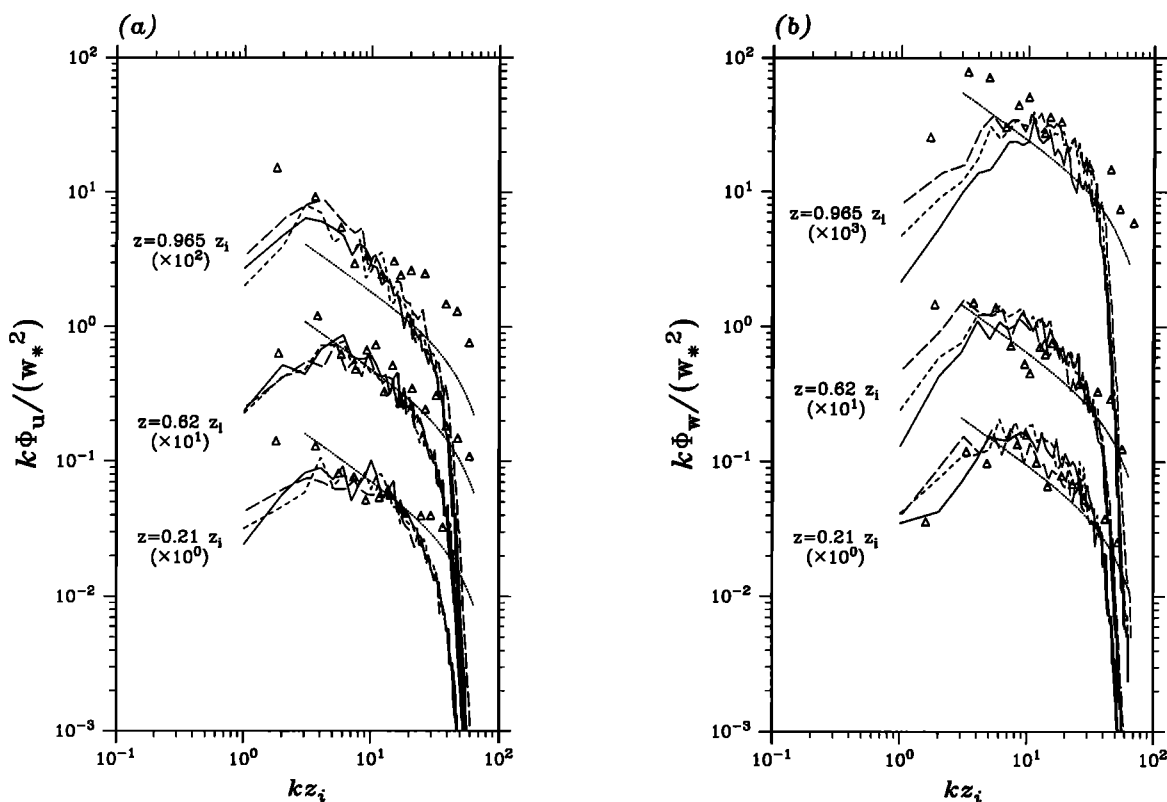


Figure 5. Normalized horizontal wavenumber spectra of (a) zonal velocity Φ_u , (b) vertical velocity Φ_w , and (c) potential temperature Φ_Θ , from the three validation experiments on day 3 at depths $z/z_i = 0.965, 0.62$, and 0.21 . The normalization, line types, and symbols are as described for Figure 3. The dotted lines indicate the theoretical inertial-convective range spectra.

$$\Phi_u(k) = \alpha_1 \langle \epsilon \rangle^{2/3} k^{-5/3}, \quad \Phi_w(k) = \frac{4}{3} \alpha_1 \langle \epsilon \rangle^{2/3} k^{-5/3},$$

$$\Phi_\Theta = \beta_1 \langle \epsilon_T \rangle \langle \epsilon \rangle^{-1/3} k^{-5/3},$$

where $\alpha_1 \approx 0.52$, $\beta_1 \approx 0.8$ [Andreas, 1987], and the subgrid dissipation rate for temperature variance is $\epsilon_T = K_h (\partial \Theta / \partial x_i)^2$ [Schmidt and Schumann, 1989]. The magnitude of the inertial subrange spectrum is therefore determined from subgrid dissipation and the diffusion of the potential temperature gradient. The model wavenumber spectra were computed in the zonal direction and ensemble averaged over all y values. The rapid drop-off of energy at the higher wavenumbers (length scales shorter than about $3.5\Delta x$) is caused by the filter that is used to remove $2\Delta x$ motions.

Here Φ_u (Figure 5a) and Φ_w (Figure 5b) are in very good agreement with the experimental data of Deardorff and Willis [1985]. For Φ_u the three validation experiments have identical shapes, with a slight magnitude increase for the V-NR experiment at depth $0.965z_i$ corresponding to the relatively higher value of $\langle u'^2 \rangle$ (Figure 3a) at the same depth. The three spectra have a peak at a wavelength of about $1.25z_i$ ($2z_i$ at depth $0.965z_i$) with a decrease in energy at longer wavelengths. For the two experiments with rotation, V-FR and V-VCR, Φ_w are nearly identical. The V-NR experiment, however, has more energy at length scales greater than $0.75z_i$ for depths 0.21 and $0.62z_i$ and higher energy at all length scales at depth $0.965z_i$. This is consistent with the higher values of $\langle w'^2 \rangle$ in the V-NR experiment below $0.2z_i$ (Figure 3b). The V-FR and V-VCR experiments show a reduction in the vertical velocity energy for length scales larger than the mixed-layer depth. The shapes of Φ_u and Φ_w for length scales smaller than the mixed-layer depth follow the shape and magnitude of the inertial subrange spectrum. In contrast, Φ_Θ (Figure 5c) is not in agreement with the laboratory data. The spectra do agree,

however, with the shape and approximate magnitude of the theoretical inertial subrange spectrum for wavelengths larger than the mixed-layer depth, an indication that the spectrum of potential temperature from the model is consistent with the turbulent mixing process. The potential temperature spectra from V-FR and V-VCR experiments are nearly identical, but the spectrum from the V-NR experiment has a higher magnitude at $0.965z_i$ and lower magnitude at $0.62z_i$.

3.4. Horizontal Component of Rotation

Selected terms in the zonal momentum equation computed in four downdraft regions of the V-FR experiment at day 3 are presented in Figure 6. Although the qualitative and quantitative differences between the V-FR and V-VCR experiments are small, $2\Omega_y w$ is of the same order of magnitude as P_x , $2\Omega_z v$, and $\partial \cdot \nabla u$, the sum of the advection terms. The $2\Omega_y w$ term is identically zero at the surface, monotonically increasing until the middle of the mixed layer, and then decreasing rapidly, where it is almost zero at the mixed-layer base. The dynamics of the downdrafts therefore require the presence of both rotation components for the correct dynamic balance.

4. Greenland Sea Experiments

The four experiments described here examine the effects of rotation and the thermobaric instability on the generation of penetrative convection. In these experiments, model initialization was based on cast CTD65, a potential temperature and salinity profile taken at 2°W , $74^\circ 45'\text{N}$ during February 1988 in the central Greenland Sea as reported by Rudels *et al.* [1989]. This profile has the vertical structure, described by Aagaard and Carmack [1989], that is essential for thermobaric instability; namely, a relatively cold fresh layer overlying warm salty water. However, the profile

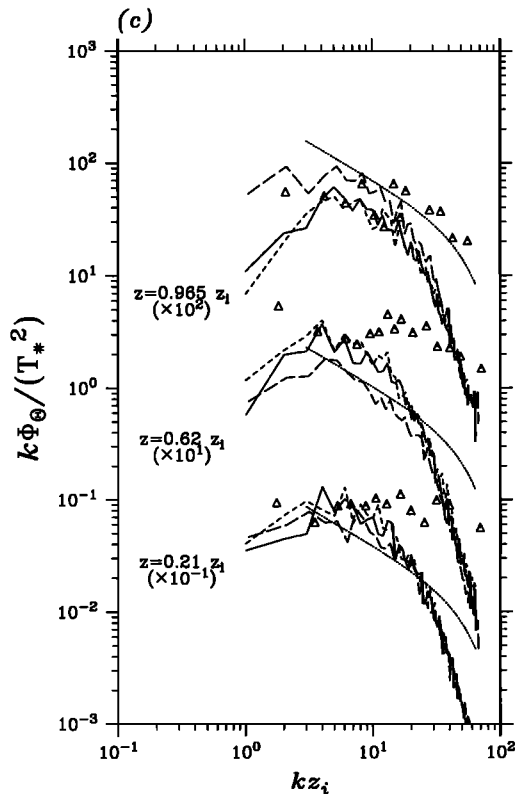


Figure 5. (continued)

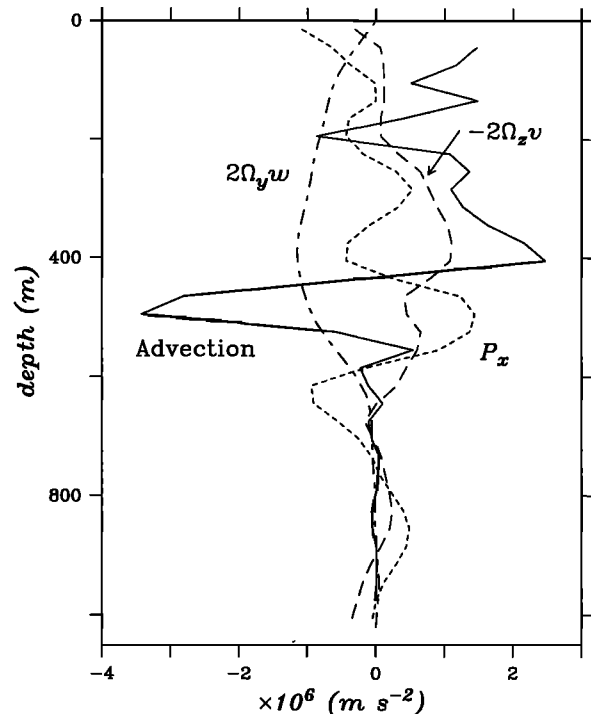


Figure 6. Ensemble and horizontally averaged selected terms of the zonal momentum equation from four downdraft regions of the V-FR experiment at day 3.

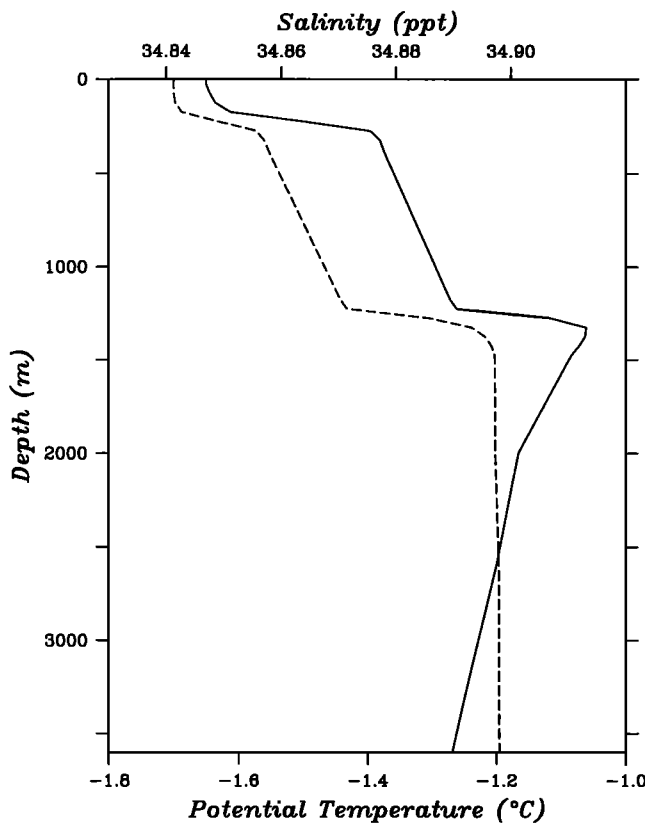


Figure 7. Initial potential temperature (solid line) and salinity (dashed line) profile based on a profile taken at 2°W, 74°45'N during February 1988 in the central Greenland Sea (Rudels *et al.*, [1989]), and used with the Greenland Sea experiments.

requires over 5 days of cooling with -300 W m^{-2} heat flux and -110 W m^{-2} latent heat flux before deep convection begins. Computational resources were conserved by creating an initialization profile from CTD65. This initialization profile (Figure 7) was created as follows: first, by initializing the model using CTD65 in a small domain; second, by forcing the model for 4 days with -300 W m^{-2} heat flux and -110 W m^{-2} latent heat flux; and finally, by horizontally averaging the potential temperature and salinity fields.

The four experiments summarized in Table 3 were performed using a variety of grid spacing, time step, rotation components, and pressure effects on density. The first experiment uses the full equation of state (EOS) for seawater and both components of the Coriolis force (GS-FR), the second experiment uses the full EOS but does not include rotation (GS-NR), the third experiment uses the full EOS but only the vertical component of the Coriolis force

(GS-VCR), and the last experiment uses a quadratic approximation to the EOS with pressure effects removed (removing the thermobaric instability) and includes full rotation (GS-NTB). A latitude of 75°N was chosen for the experiments with rotation. The surface forcing for all experiments includes a heat flux of -300 W m^{-2} , a latent heat flux of -110 W m^{-2} , and no wind stress. Model spin-up was facilitated by the addition of a random pattern to the heat flux for the first 2 hours. The heat flux and latent heat flux are typical values from the region during winter; however, we chose to not apply a wind stress to simplify the analysis.

In the GS-FR, GS-NR, and GS-VCR experiments a domain size of 5000 m in the zonal and meridional directions and 3600 m in the vertical and a run length of 6 days for a total of 5184 time steps were used. The model fields were written every 6 hours the first day, every hour the next 2 days, and every 4 hours during the last 3 days. For the GS-NTB experiment a domain size of 3000 m in the zonal and meridional directions and 3600 m in the vertical and a run length of 6 days for a total of 4320 time steps were used. Model fields were written every 6 hours during the entire 6 days. Our analysis of the Greenland Sea experiments concentrates on results from day 2, when penetrative convection is dominant, and day 6, when CML deepening is dominant. These 2 days are a good representation of the evolution of convection that occurs during the experiments.

A summary of the scales and nondimensional numbers for the GS-FR and GS-VCR experiments is presented in Table 4. These estimates were made for day 6 since convective mixed-layer deepening dominates the motions at that time. The values of Ra_f and Ta place these experiments in the geostrophic turbulence regime [Bouhnov and Golitsyn, 1990]. The depth at which potential temperature variance $\langle \Theta^2 \rangle$ begins to increase rapidly (Figure 8) was chosen as an estimate of z_i , the mixed-layer depth (z_i can also be estimated from $\langle \Theta \rangle$ and $\langle w' \Theta' \rangle$). The values of K_m and K_h are computed by averaging over the mixed-layer depth and the horizontal extent of the model domain.

Since $z_c \approx z_i$, we conclude for the Greenland Sea experiments that the convection is affected by rotation and that therefore u_r and D are the suitable scales for velocity and space, respectively. When rotation is important, $(H/l_p)^2 \ll 1$ is required for the hydrostatic approximation to be valid [Jones and Marshall, 1993], where H , the vertical scale of motion, is z_i , the mixed-layer depth, for convective mixed-layer deepening. However, the value of $(z_i/l_p)^2$ indicates that the flow is nonhydrostatic (Table 4).

4.1. Instantaneous Fields

The three-dimensional structure of Θ for the GS-FR experiment at day 2 is illustrated in Plate 3. The color scale was adjusted to facilitate the visualization of the penetrative plumes. The number of plumes decreases rapidly with depth, and the deepest plumes

Table 3. Greenland Sea Experiment Summary

Experiment	$\Omega_z = 0$	$\Omega_y = 0$	$\frac{\partial p}{\partial P} = 0$	Δx , m	Grid	Δt , s	Comments
GS-FR	no	no	no	50	100×100×72	100	full rotation
GS-NR	yes	yes	no	50	100×100×72	100	no rotation
GS-VCR	yes	no	no	50	100×100×72	100	vertical component of rotation only
GS-NTB	no	no	yes	60	50×50×60	120	no thermobaric effect

Variables are defined as follows: Ω_z , vertical component of the Coriolis parameter; Ω_y , horizontal component of the Coriolis parameter; $\partial p / \partial P$, density change with pressure; Δx , grid spacing; Δt , time step.

Table 4. Scales and Nondimensional Numbers for the GS-FR and GS-VCR Experiments for Day 6

Variable	Value
z_i , m	1300
z_c , m	1495
D , m	2034
l_p , m	391
$(z_i/l_p)^2$	11
T^* , °C	0.002
Ra_f	4×10^9
Ta	2×10^8
w_* , m s ⁻¹	0.037
u_* , m s ⁻¹	0.066
Ro^*	0.091
K_m , m ² s ⁻¹	0.015
K_b , m ² s ⁻¹	0.045
α , °C ⁻¹	3.1×10^{-5}
β , psu ⁻¹	7.9×10^{-4}
ρ_0 , kg m ⁻³	1028.18

Conditions on day 6 were as follows: buoyancy flux $B_0 = 3.8 \times 10^{-8} \text{ m}^2 \text{ s}^{-3}$, Coriolis parameter $f = 1.4 \times 10^{-4} \text{ s}^{-1}$, reference potential temperature $\Theta_0 = -1.6^\circ \text{C}$, and reference salinity $S_0 = 35$ psu.

can be seen to penetrate through regions of stably stratified water. The plume diameter does not substantially increase as a function of depth. Many plumes travel downward at a definite angle from the vertical because of the horizontal component of the Earth's rotation. In contrast, CML deepening is qualitatively different (Plate 1). The plumes are more diffuse, quickly lose their Θ difference with the ambient fluid, and do not penetrate very far into stably stratified fluid.

The horizontal structure of Θ , w , and \bar{e}'' is presented for GS-FR (Plate 4a) and GS-NR (Plate 4b) for model day 2. Active penetrative convection is characterized by regions of strong downward w in conjunction with a Θ that is below the ambient value and has a relatively high value of \bar{e}'' . Typical values of w in the plumes are -0.05 to -0.09 m s^{-1} and, outside the plumes, a maximum of about 0.02 m s^{-1} . Schott *et al.* [1993] have reported from measurements from the central Greenland Sea during March 1989 a vertical propagation of plume events of -0.08 m s^{-1} .

Penetrative convection is well developed for both the GS-FR and GS-NR experiments as shown by the nearly constant plume diameter from 675 to 975 m depth. This is in agreement with the analytical results of T. Paluszkievicz and R. Romea (A one-dimensional model for the parameterization of deep convection in the ocean, submitted to *Dynamics of Atmospheres and Oceans*, 1995) of the plume structure of thermobaric instability. The distributed source of buoyancy made available from the thermobaric instability accelerates the plume downward, and mass conservation balanced with diffusion creates a plume shape that is

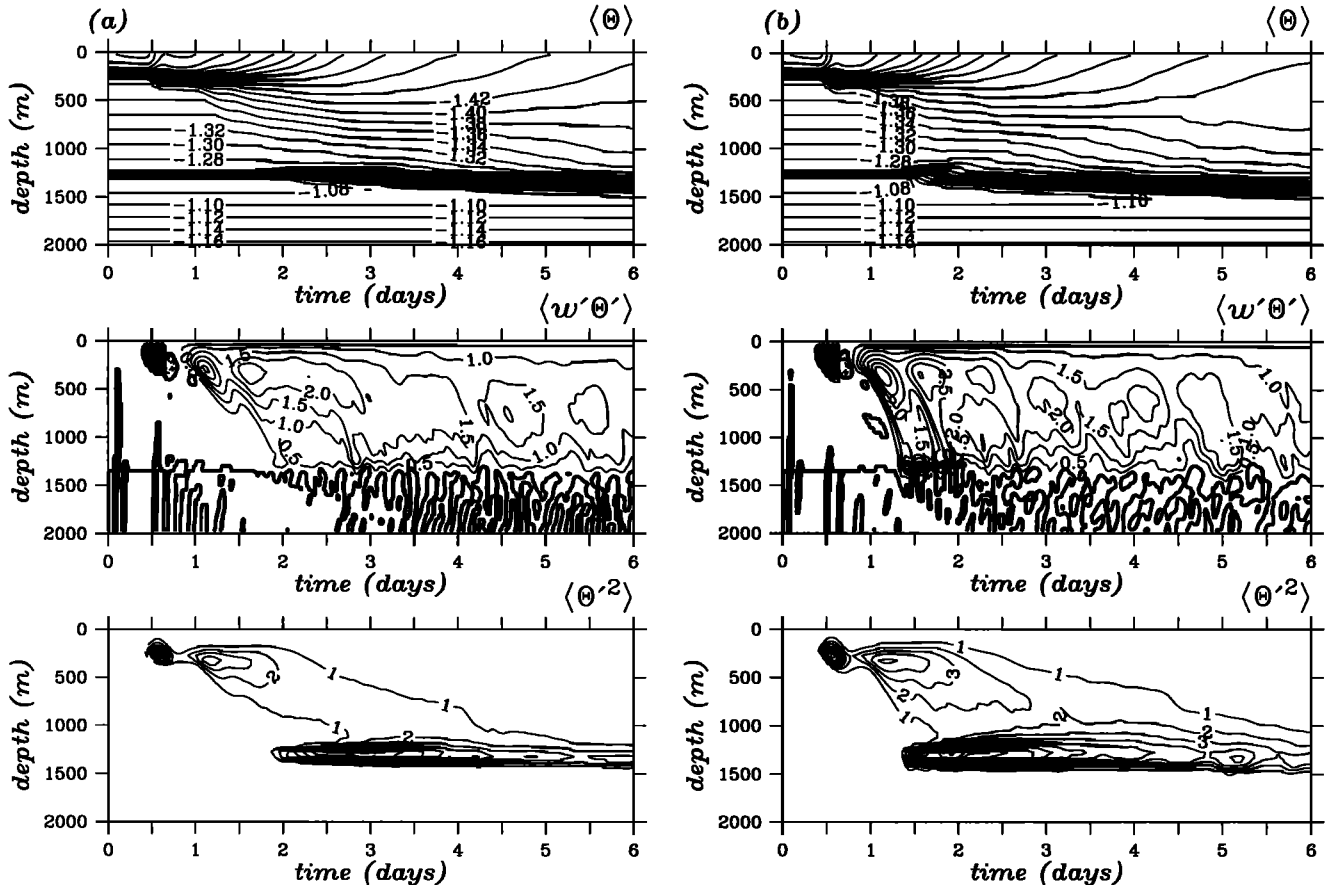


Figure 8. Horizontally averaged (top) potential temperature $\langle \Theta \rangle$, (middle) heat flux $\langle w' \Theta' \rangle$, and (bottom) potential temperature variance $\langle \Theta'^2 \rangle$ as a function of depth and time for the Greenland Sea (GS) experiments (a) GS-FR, (b) GS-NR, and (c) GS-NTB. Here $\langle w' \Theta' \rangle$ and $\langle \Theta'^2 \rangle$ are multiplied by 10^4 and 10^3 , respectively, for display purposes. Contour intervals for $\langle \Theta \rangle$, $\langle w' \Theta' \rangle$, and $\langle \Theta'^2 \rangle$ are 0.02°C , $0.5 \times 10^{-4}^\circ \text{C m s}^{-1}$, and $1 \times 10^{-3}^\circ \text{C}^2$, respectively.

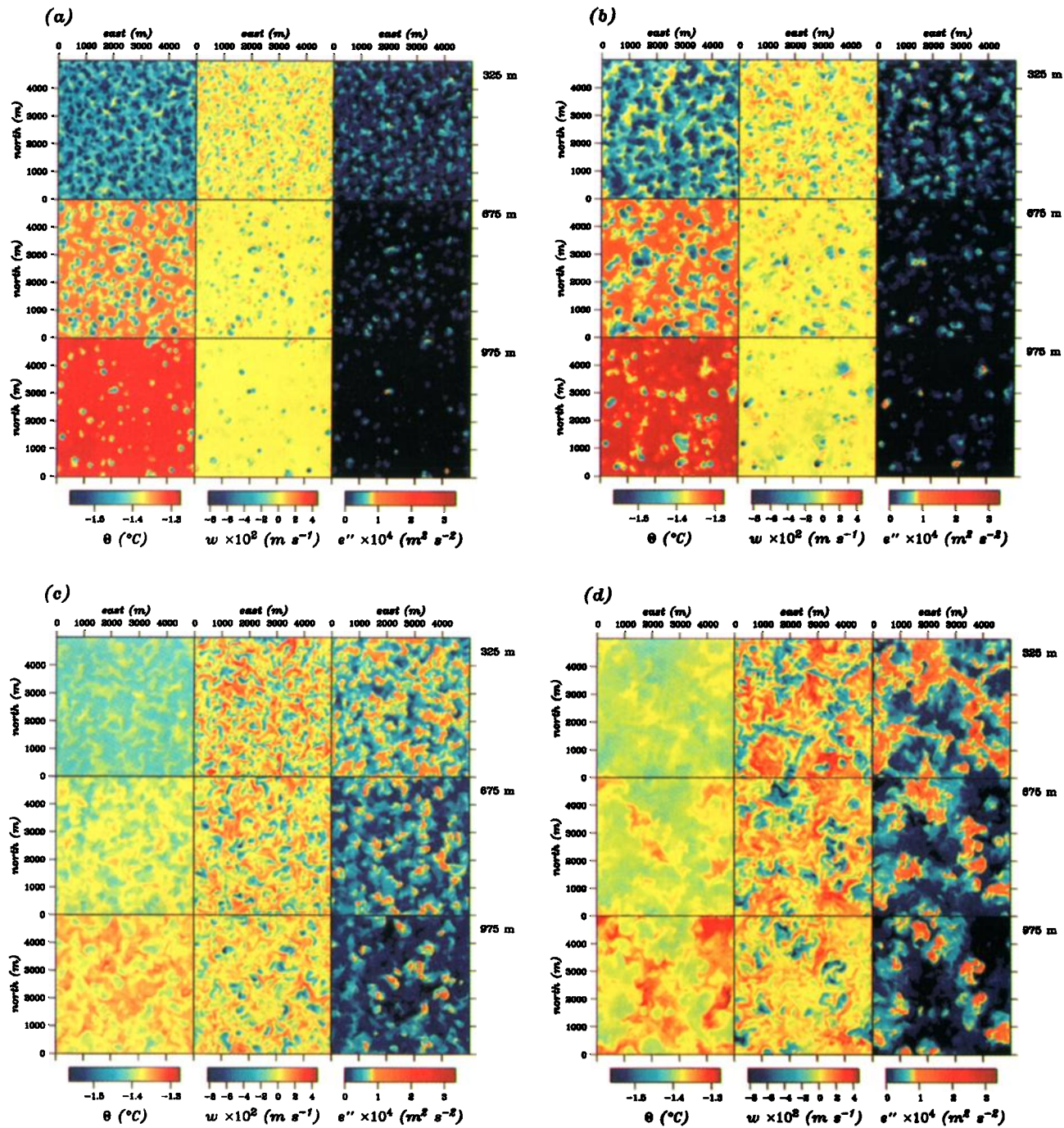


Plate 4. Horizontal sections from the Greenland Sea experiments, (a) GS-FR at day 2, (b) GS-NR at day 2, (c) GS-FR at day 6, and (d) GS-NR at day 6, of potential temperature Θ , vertical velocity w , and subgrid turbulent kinetic energy e'' at depths $z = 325, 675$, and 975 m. Here w and e'' have been multiplied by 10^2 and 10^4 , respectively, for display purposes.

structures for GS-NR (Plate 4d) are about 5000 m in length and 500 m wide at 325 m depth and about 5000 m in length and 1000 m wide at 975 m depth. The differences in scales show that, at this time, the presence of rotation greatly restricts the size of the convective elements.

4.2. Horizontal Component of Rotation

The effect of the horizontal component of the Coriolis force is shown by the velocity structure near the head of a penetrative plume (Figure 9). An isolated plume near the start of penetrative

convection was chosen for the GS-FR (Figure 9a), GS-NR (Figure 9b), and GS-VCR (Figure 9c) experiments in order to minimize the effect of circulations created by other plumes. The horizontal velocity fields at 975 m depth are presented for each experiment. Without planetary rotation (GS-NR) the model flow is radially outward and symmetric about the plume axis. The GS-VCR experiment, with the vertical component of rotation, has a velocity structure that is also symmetric about the plume axis but with a clockwise rotation superimposed on the radially outward flow. Finally, the GS-FR experiment, with both components of

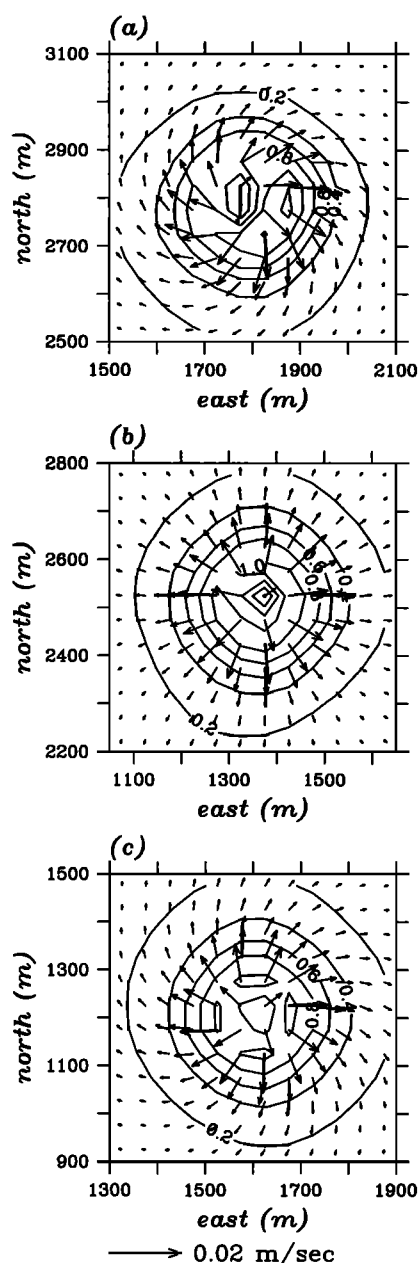


Figure 9. Horizontal sections 600 m on a side taken from the (a) GS-FR, (b) GS-NR, and (c) GS-VCR experiments of horizontal velocity \vec{u} , and speed (contours) at 975 m depth and days 1.375, 1.3, and 1.333, respectively. Values for speed are multiplied by 10^2 for display purposes, and the contour interval is $0.2 \times 10^{-2} \text{ m s}^{-1}$.

rotation present, has the most complex flow; the flow is similar to that from the GS-VCR experiment, but with stronger flow to the east and south. The strong negative vertical velocity in the plume creates an eastward acceleration via the $-2\Omega_z w$ term in the u momentum equation; this stronger eastward flow then causes a southward acceleration via the $-2\Omega_z u$ term in the v momentum equation.

4.3. Mean Profiles

The mean profiles of $\langle \Theta \rangle$, $\langle w'\Theta' \rangle$, and $\langle \Theta'^2 \rangle$ are displayed as functions of depth and time in Figure 8. This presentation highlights the evolution of the fields and the differences between

the periods of penetrative convection and CML deepening. The qualitative and quantitative differences between the GS-FR and GS-VCR experiments are small as was the case in the validation experiments; therefore the results for the GS-VCR experiment are not presented in this section. However, the differences between GS-FR (Figure 8a), GS-NR (Figure 8b), and GS-NTB (Figure 8c) are significant as demonstrated in the $\langle \Theta \rangle$, $\langle w'\Theta' \rangle$, and $\langle \Theta'^2 \rangle$ fields. The peak in $\langle w'\Theta' \rangle$ and $\langle \Theta'^2 \rangle$ in the mixed layer at day 0.5 for the GS-FR and GS-NR experiments is a transient produced during the spin-up of the model. This transient behavior is absent by model day 0.75.

The onset of plumes for the GS-FR and GS-NR experiments occurs at approximately the same time. However, GS-FR has smaller values of $\langle w'\Theta' \rangle$, and the evolution of this quantity occurs more slowly for GS-FR: the $0.5 \times 10^{-4} (\text{°C m s}^{-1})$ contour reaches 1200 m depth almost one-half day later than for GS-NR. At 1300 m depth, $\langle \Theta'^2 \rangle$ also starts a rapid increase in GS-FR almost one-half day later than for GS-NR. A period of strong penetrative convection begins at approximately day 1.5 and continues through day 2.5. This period is indicated by values of $\langle w'\Theta' \rangle$ greater than $2 \times 10^{-4} (\text{°C m s}^{-1})$ and the presence of a second maximum of $\langle \Theta'^2 \rangle$ that is shallower than the large peak at 1300 m depth. After the period of strong penetrative convection, the CML deepening in GS-NR is still more rapid than that in GS-FR. For example, the surfacing of the -1.44°C isotherm occurs at day 5.1 for GS-FR and day 3.9 for GS-NR.

The behavior of the strong vertical gradient of $\langle \Theta \rangle$ at 1300 m depth is another example of the differences between GS-FR and GS-NR. In both experiments, overshooting plumes cause mixing below the thermocline. The amount of mixing is stronger for the GS-NR case. For example, the -1.08°C isotherm in the GS-NR experiment is mixed out at day 1.5 and the -1.1°C isotherm is not mixed out until day 3 and the -1.08°C isotherm is not mixed out within the 6-day model run. The swiftness of the thermocline broadening in the GS-NR experiment is an indication of the greater strength of the vertical motions for this experiment.

Large differences in the mean fields between the experiments that include the effects of pressure on density (GS-FR and GS-NR) and the experiment that does not include this effect (GS-NTB) are noted. The combined effect of Θ , S , and P on the compressibility of seawater is required for thermobaric instability [Aagaard and Carmack, 1989]. During the GS-NTB experiment, penetrative plumes are not produced, and therefore the mixed-layer depth increases more gradually via CML deepening, whereas for GS-FR and GS-NR the mixed-layer depth increases abruptly because of penetrative plumes. The evolution of $\langle \Theta \rangle$, $\langle w'\Theta' \rangle$, and $\langle \Theta'^2 \rangle$ for GS-NTB is more typical of CML deepening.

4.4. Spectra

Several differences between strong penetrative convection and CML deepening are illustrated by Φ_w , presented at day 2 (Figure 10a) and day 6 (Figure 10b) for the GS-FR (solid line), GS-NR (long-dashed line), and GS-VCR (short-dashed line) experiments. The spectral levels for all three experiments are 5 times higher at day 6 than at day 2. For the GS-FR and GS-VCR experiments the wavelength of the spectral peak shifts from 400 m at day 2 to 600 m at day 6, indicating a small change in the scale of the convective structures. For GS-NR, however, the wavelength of the spectral peak shifts from 600 m at day 2 to 2500 m at day 6, which is a very large change in the scale of the convective features.

The inertial subrange spectrum (dotted line) is about one decade lower than the experimental results at day 2 (Figure 10a). The

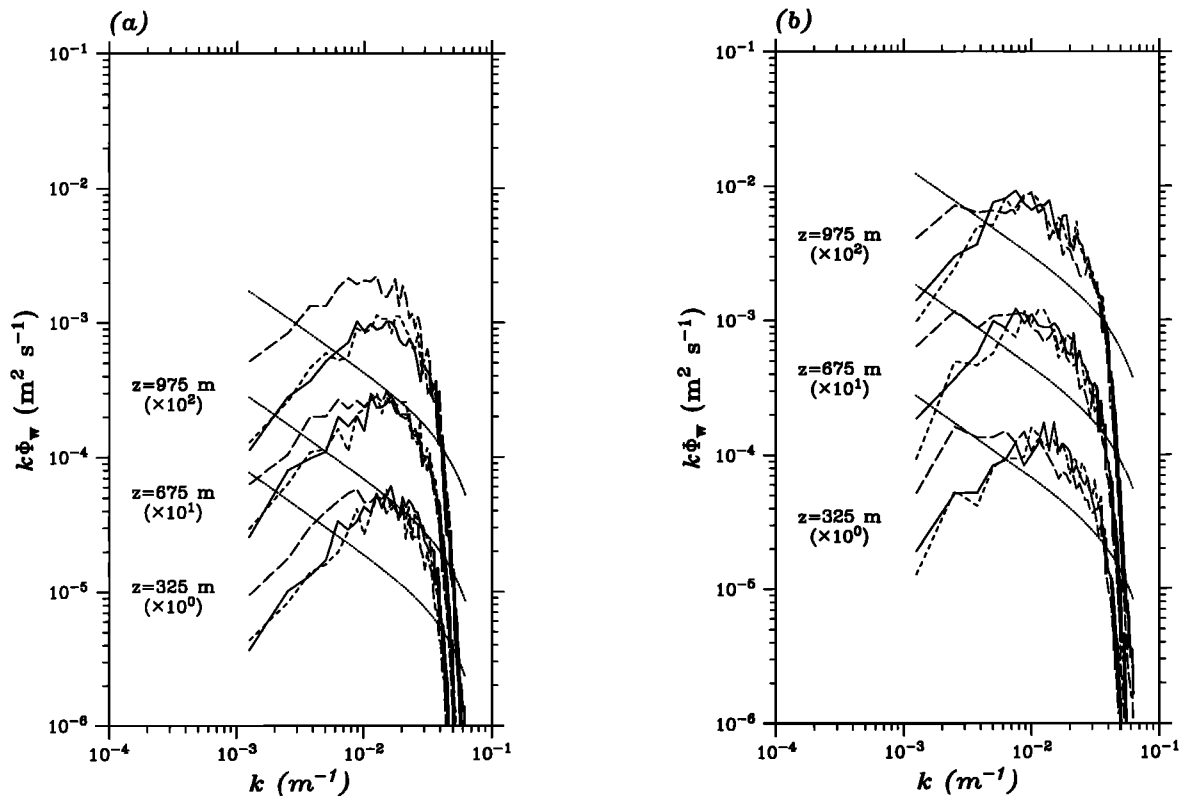


Figure 10. Horizontal wavenumber spectra of vertical velocity Φ_w at 325, 675, and 975 m depth for (a) day 2, and (b) day 6 from the Greenland Sea experiments, GS-FR (solid line), GS-NR (long-dashed line) and GS-VCR (short-dashed line). The dotted lines indicate the theoretical inertial-convective range spectra.

theoretical forms of $\langle \epsilon \rangle$ and $\langle \epsilon_T \rangle$ used in adjusting the level of the spectrum were developed assuming the flow is isotropic and homogeneous. During the period of strong penetrative convection, the resolved motions are clearly not consistent with these assumptions. However, the spectra do have the shape of the inertial subrange spectrum for wavelengths less than 600 m. At day 6 the inertial subrange spectra are in much better agreement with both the magnitude and shape of the three experiments for wavelengths less than about 1000 m. This improved agreement indicates that the motions have evolved from the penetrative convection at day 2 to a homogeneous, isotropic, mixed-layer deepening by day 6.

5. Summary

OLEM was constructed in order to study the processes important in deep convection. To accomplish this, a large-eddy simulation approach was followed to resolve the scales of the important motions. Because of the velocity and length scales of deep convection, both components of the Coriolis force, the nonhydrostatic terms in the vertical momentum equation, and the full nonlinear equation of state were required. The finite difference implementation uses cyclic horizontal boundary conditions, rigid lid, flat bottom, and surface forcing via total heat flux, latent heat flux, and wind stress.

The validation experiments demonstrate the ability of OLEM to accurately reproduce mean profiles of zonal, vertical, and potential temperature variance and heat flux from laboratory measurements of Willis and Deardorff [1974] and Deardorff and Willis [1985] and from aircraft measurements of the atmospheric convective boundary layer by Lenschow et al. [1980]. The horizontal

wavenumber spectra of zonal and vertical velocities are in excellent agreement with the laboratory data of Deardorff and Willis [1985] and the theoretical inertial subrange spectrum. The effect that Earth's rotation has on convection is clearly demonstrated in the vertical velocity variance profile, vertical velocity spectra, and the horizontal sections of potential temperature, vertical velocity, and subgrid kinetic energy. In the absence of rotation the vertical motions are more energetic and the convective motions are more organized. The overall qualitative and quantitative effect of the horizontal component of the Coriolis force is small. However, it is significant in the downdrafts and therefore cannot be completely ignored.

The Greenland Sea experiments were performed to determine the effect of the thermobaric instability and rotation on the structure and evolution of deep convection. The artificial removal of the thermobaric instability suppresses the generation of penetrative convection such that only CML deepening occurs. The downward propagation of penetrative plumes creates rapid changes in $\langle \Theta \rangle$, $\langle w'\Theta' \rangle$, and $\langle \Theta'^2 \rangle$ at depths much greater than occurs for CML deepening. The penetrative plumes have maximum velocities of -0.08 m s^{-1} and diameters of 300 m, which are in good agreement with estimates from Schott et al. [1993]. For the experiments with thermobaric instability, strong penetrative convection begins at day 1.5 and continues for 1 day. This is followed by a gradual transition to CML deepening as the thermobaric instability becomes less dominant. During the period of strong penetrative convection the values of $\langle w'\Theta' \rangle$ and $\langle \Theta'^2 \rangle$ are about 2 and 4 times greater, respectively, than during CML deepening; however, maximum values of Φ_w are 5 times greater during CML deepening. Although CML deepening has more

energetic vertical motions, **vertical heat transport is greater during penetrative convection**. The evolution of penetrative convection occurs more rapidly, and vertical motions are more vigorous in the absence of rotation. The horizontal component of rotation causes asymmetries in the circulation around a single penetrative plume, even though the mean properties of the flow are not significantly affected. This asymmetry in the clockwise rotating current can cause a southeastward slant to the penetrative plumes.

These experiments clearly demonstrate the importance of thermobaric instability and rotation on deep convection. **Thermobaric instability, in turn, supports the existence of deep penetrative convection, which is capable of rapidly altering water properties at great depth.** To properly model large-scale flows in regions of penetrative convection, it is necessary to include the effects of penetrative convection in the vertical mixing parameterization. Such a parameterization must be able to move water parcels vertically to great depths without substantial mixing at the intermediate depths.

Acknowledgments. The authors wish to thank Michael R. Riches, acting director of the Environmental Sciences Division of the Office of Health and Environmental Research, for his continual support of this work. This study was carried out under the auspices of the CO₂ Oceans Program at the Battelle/Marine Sciences Laboratory. The Battelle/Marine Sciences Laboratory is part of the Pacific Northwest National Laboratory, which is operated for the U.S. Department of Energy by Battelle Memorial Institute under contract DE-AC06-76RLO 1830.

References

- Aagaard, K., and E. C. Carmack, The role of sea ice and other fresh water in the Arctic circulation, *J. Geophys. Res.*, **94**, 14,485-14,498, 1989.
- Andreas, E. L., Spectral measurements in a disturbed boundary layer over snow, *J. Atmos. Sci.*, **44**, 1912-1939, 1987.
- Boubnov, B. M., and G. S. Golitsyn, Temperature and velocity field regimes of convective motions in a rotating plane fluid layer, *J. Fluid Mech.*, **219**, 215-239, 1990.
- Clarke, R. A., and J. C. Gascard, The formation of Labrador Sea water, I, Large-scale processes, *J. Phys. Oceanogr.*, **13**, 1764-1778, 1983.
- Colella, P., Multidimensional upwind methods for hyperbolic conservation laws, *J. Comput. Phys.*, **87**, 171-200, 1990.
- Deardorff, J. W., Numerical investigation of neutral and unstable planetary boundary layers, *J. Atmos. Sci.*, **29**, 91-115, 1972.
- Deardorff, J. W., The use of subgrid transport equations in a three-dimensional model of atmospheric turbulence, *J. Fluids Eng.*, **95**, 429-438, 1973.
- Deardorff, J. W., Stratocumulus-capped mixed layers derived from a three-dimensional model, *Boundary Layer Meteorol.*, **18**, 495-527, 1980.
- Deardorff, J. W., and G. E. Willis, Further results from a laboratory model of the convective planetary boundary layer, *Boundary Layer Meteorol.*, **32**, 205-236, 1985.
- Fernando, H. J. S., D. L. Boyer, and R. Chen, Turbulent thermal convection in rotating and stratified fluids, *Dyn. Atmos. Oceans*, **13**, 95-121, 1989.
- Fernando, H. J. S., R. Chen, and D. L. Boyer, Effects of rotation on convective turbulence, *J. Fluid Mech.*, **228**, 513-547, 1991.
- Garwood, R. W., S. M. Isakari, and P. C. Gallacher, Thermobaric convection, in *The Polar Ocean and Their Role in Shaping the Global Environment*, *Geophys. Monogr. Ser.*, vol. 85, edited by O. Johannessen, R. Muench, and J. Overland, pp. 199-209, AGU, Washington, D. C., 1994.
- Gascard, J. C., and R. A. Clarke, The formation of Labrador Sea water, II, Mesoscale and smaller-scale processes, *J. Phys. Oceanogr.*, **13**, 1779-1797, 1983.
- Gordon, A. L., Deep Antarctic convection west of Maud Rise, *J. Phys. Oceanogr.*, **8**, 600-612, 1978.
- Gordon, A. L., Weddell Deep Water variability, *J. Mar. Res.*, **40**, 199-217, 1982.
- Harlow, F. H., and J. E. Welch, Numerical calculation of time-dependent viscous incompressible flow of fluid with free surface, *Phys. Fluids*, **8**, 2182-2189, 1965.
- Heinze, C., P. Schlosser, K. P. Koltermann, and J. Meincke, A tracer study of the deep water renewal in the European polar seas, *Deep Sea Res., Part A*, **37**, 1425-1453, 1990.
- Jones, H., and J. Marshall, Convection with rotation in a neutral ocean: A study of open-ocean deep convection, *J. Phys. Oceanogr.*, **23**, 1009-1039, 1993.
- Killworth, P. D., The mixing and spreading phases of MEDOC, I, *Prog. Oceanogr.*, **7**, 59-90, 1976.
- Killworth, P. D., On 'chimney' formations in the ocean, *J. Phys. Oceanogr.*, **9**, 531-554, 1979.
- Lenschow, D. H., J. C. Wyngaard, and W. T. Pennell, Mean-field and second-moment budgets in a baroclinic, convective boundary layer, *J. Atmos. Sci.*, **37**, 1313-1326, 1980.
- Madec, G., M. Chartier, P. Delecluse, and M. Crépon, A three-dimensional numerical study of deep-water formation in the northwestern Mediterranean Sea, *J. Phys. Oceanogr.*, **21**, 1349-1371, 1991.
- Manabe, S., and R. J. Stouffer, Two stable equilibria of coupled ocean-atmosphere model, *J. Clim.*, **1**, 841-866, 1988.
- Mason, P. J., Large-eddy simulation: A critical review of the technique, *Q. J. R. Meteorol. Soc.*, **120**, 1-26, 1994.
- Maxworthy, T., and S. Narimousa, Unsteady deep convection in a homogeneous rotating fluid, *J. Phys. Oceanogr.*, **24**, 865-887, 1994.
- McDougall, T. J., Thermobaricity, cabelling, and water-mass conversion, *J. Geophys. Res.*, **92**, 5448-5464, 1987.
- McWilliams, J. C., P. C. Gallacher, C.-H. Moeng, and J. C. Wyngaard, Modeling the oceanic planetary boundary layer, in *Large Eddy Simulation of Complex Engineering and Geophysical Flows*, edited by Boris Galperin and Steven A. Orszag, pp. 441-454, Cambridge Univ. Press, New York, 1993.
- Moeng, C.-H., A large-eddy-simulation model for the study of planetary boundary-layer turbulence, *J. Atmos. Sci.*, **41**, 2052-2062, 1984.
- Raasch, S., and D. Etling, Numerical simulation of rotating turbulent thermal convection, *Contrib. Atmos. Phys.*, **64**, 185-200, 1991.
- Rhein, M., Ventilation rates of the Greenland and Norwegian seas derived from distributions of the chlorofluoromethanes F11 and F12, *Deep Sea Res., Part A*, **38**, 485-503, 1991.
- Rudels, B., D. Quadfasel, H. Friedrich, and M.-N. Houssais, Greenland Sea convection in the winter of 1987-1988, *J. Geophys. Res.*, **94**, 3223-3227, 1989.
- Schmidt, H., and U. Schumann, Coherent structure of the convective boundary layer derived from large-eddy simulations, *J. Fluid Mech.*, **200**, 511-562, 1989.
- Schott, F., M. Visbeck, and J. Fischer, Observations of vertical currents and convection in the central Greenland Sea during the winter of 1988-1989, *J. Geophys. Res.*, **98**, 14,401-14,421, 1993.
- Siegel, D. A., and J. A. Domaradzki, Large-eddy simulation of decaying stably stratified turbulence, *J. Phys. Oceanogr.*, **24**, 2353-2386, 1994.
- Skyllingstad, E. D., and D. W. Denbo, An ocean large-eddy simulation of Langmuir circulations and convection in the surface mixed layer, *J. Geophys. Res.*, **100**, 8501-8522, 1995.
- van Leer, B., Towards the ultimate conservative difference scheme, IV, A new approach to numerical convection, *J. Comput. Phys.*, **23**, 276-299, 1977.
- Washington, W. M., and G. A. Meehl, Climate sensitivity due to increased CO₂: Experiments with a coupled atmosphere and ocean general circulation model, *Clim. Dyn.*, **4**, 1-38, 1989.
- Willis, G. E., and J. W. Deardorff, A laboratory model of the unstable planetary boundary layer, *J. Atmos. Sci.*, **31**, 1297-1307, 1974.
- Wyngaard, J. C., O. R. Cote, and K. S. Rao, Modeling the atmospheric boundary layer, *Adv. Geophys.*, **18A**, 193-211, 1974.

D. W. Denbo (corresponding author) and E. D. Skyllingstad, Pacific Northwest National Laboratory, 1529 West Sequim Bay Road, Sequim, WA 98382. (email: dwd@mystery.pnl.gov; eds@windfall.pnl.gov)

(Received December 8, 1993; revised July 19, 1995; accepted September 14, 1995.)